applied sciences

MDPI

Article

Simultaneous Adsorption and Photocatalysis Processes Based on Ternary TiO_2–Cu_xS–Fly Ash Hetero-Structures

Luminita Andronic [1,*], Luminita Isac [2], Cristina Cazan [2] and Alexandru Enesca [1]

[1] Product Design, Mechatronics and Environment Department, Transilvania University of Brasov, 500036 Brasov, Romania; aenesca@unitbv.ro

[2] Renewable Energy Systems and Recycling Research Center, Transilvania University of Brasov, 500036 Brasov, Romania; isac.luminita@unitbv.ro (L.I.); c.vladuta@unitbv.ro (C.C.)

* Correspondence: andronic-luminita@unitbv.ro

Received: 19 October 2020; Accepted: 10 November 2020; Published: 13 November 2020

Featured Application: Based on the present experimental results, which consider satisfactory photocatalytic degradation activity and good charge separation, the ternary heterostructures can be further tested in a dynamic system for wastewater treatment applications.

Abstract: Ternary composites of TiO_2–Cu_xS–fly ash were used in simultaneous adsorption and photocatalysis processes for the removal of organic (dye) pollutants. Composites of semiconductor (TiO_2, Cu_xS) nanomaterials hosted within matrices of fly ash, such as film heterostructures, are promising materials for advanced wastewater treatment. The combination of adsorption and photocatalysis processes was investigated in the removal of methylene blue (MB), considered as a standard in photocatalysis. Ternary film heterostructures obtained by doctor blade technique allows overcoming the separation step of particles from treated wastewater. The comparison between the adsorption and photodegradation tests performed with TiO_2–Cu_xS–fly ash showed that in dark conditions, the MB removal was 75% after 360 min, while in the presence of UV radiation, almost total dismissal of MB was achieved in the same treatment period. The degradation rate of MB, when H_2O_2 is used as an electron acceptor, could reach 90% in adsorption and 99% in simultaneous adsorption/photocatalysis processes. The adsorption isotherm was found to follow the Langmuir and Freundlich models.

Keywords: heterostructures; interface control; morphology optimisation; adsorption; photocatalysis

1. Introduction

Fly ash is a by-product generated by coal-fired power plants generating electricity, which is one of the earth's most significant sources of air pollution worldwide and leads to waste management proposals [1].

Nowadays, fly ash can be recycled and reused in different engineering applications, in the cement industry and in wastewater heavy metal adsorption, reducing environmental footprint [2]. The wastewater from industry and householders has a multi-pollutants composition requiring simultaneous advanced treatment processes, such as adsorption and photocatalysis [3]. These processes can be performed sequentially, with the disadvantage that they increase the technological costs [4,5]. The integration of adsorption and photocatalysis in a one-step treatment process can enhance the overall removal efficiency [6]. Advanced oxidation processes (AOPs) represent a suitable alternative to the traditional organic removal methods in terms of sustainability [7]. Various photocatalysts were studied in AOP, starting with monocomponent structures such as TiO_2 [8,9], ZnO [10,11], SnO_2 [12,13],

and WO_3 [14,15], which have the disadvantage of limited light absorption range [16,17], low chemical stability [18,19], and high charge carriers recombination rate [20,21]. In order to overcome these issues, complex photocatalysts multi-component structures based on metal oxides [22], metal sulphur [23], graphene [24], and polymers [25] were reported. Coupling semiconductors (oxide and sulfide) with a clear difference between the valence band and conduction band energies (the two difference-shifts being in the same direction) is a common strategy to minimise recombination [26]. These materials have relatively good photocatalytic efficiency, but the competition between adsorption and photocatalytic degradation should be optimised in order to decrease the operation time and to increase the materials lifetime. The heterojunctions are used as photocatalyst due to their carrier-injecting ratio properties, improved light excitation response, and efficient separation of photoexcited electron-hole pairs, inducing a higher photocatalytic reaction rate and overall output [27]. However, there are still issues related to the treatment of highly concentrated organic pollutants, which can not be avoided based only on photocatalytic processes.

A range of VIS-active photocatalysts is those based on tandem or diode type structures, displaced by the association of two semiconductors (n-n type or n-p type). These materials are relatively good adsorption substrates, but the competition between the two processes should be optimised so that the adsorption of organic compounds to be followed by photolysis and adsorption of inorganic compounds does not distort the properties of VIS-activated photocatalyst.

Titanium dioxide was largely investigated as the photocatalyst for wastewater pollutant decontamination [28], although the process efficiency is low under VIS irradiation [29,30] due to the bandgap of 3.2 eV and easy recombination of the generated hole and electrons pairs [31]. Several paths are followed: (i) properties that have an impact in photocatalysis, including chemistry defects about electronic structure, semiconductor properties, composition, and morphology, will be optimised; (ii) TiO_2 must be coupled with other semiconductors and designed multi-layered materials [32], such as TiO_2/Cu_xS [33], ZnO/TiO_2 [34], WO_3/TiO_2 [35], TiO_2/Fe_2O_3, [36], and TiO_2/SnO_2 [37]. Coupling semiconductors (oxide and/or sulfide) with a clear difference between the energy of the valence bands as well as between the energy of the conduction bands (the two difference-shifts being to the same direction) is a common strategy to minimise recombination.

Ternary materials for wastewater treatment are also investigated by other authors: MoS_2/g-C_3N_4/graphene oxide (GO) [38], reduced graphene (rGO)/TiO_2/ZnO [39], TiO_2-Au-CdS [40], Fe_3O_4@TiO_2/reduced graphene [41], TiO_2/WO_3/g-C_3N_4 [42] $Fe_3O_4/TiO_2/SiO_2$ from industrial fly ash as starting materials [43], α-Fe_2O_3-TiO_2/fly ash cenospheres [44], SnO_2-TiO_2/fly ash cenospheres [45], g-C_3N_4/N-TiO_2/Fly Ash Cenospheres [46], Fly ash/Cu/TiO_2 [47].

Therefore, the paper proposes an approach based on the removal of organic wastewater pollutants using simultaneous photocatalysis and adsorption processes. These technologies will simplify the treatment process but require good control of the key parameters. The ternary TiO_2–Cu_xS–fly ash structure was developed considering a future implementation in large scale applications, requiring (a) simple fabrication methods, (b) possibility to tailor the morphology, (c) sustainability and (d) good chemical stability. The heterostructure materials were selected based on the composition and crystalline structure compatibility.

2. Materials and Methods

2.1. Materials Preparation

The ternary TiO_2–Cu_xS–fly ash heterostructures were obtained by mixing three types of fly ash–TiO_2 (FA–TiO_2) powders, synthesized by hydrothermal method, and Cu_xS powder synthesized by photochemical precipitation. The raw fly ash is a class "F" fly ash (FA), collected from the Central Heat and Power (CHP) Plant Brasov (Brasov, Romania) [48]. The powders' synthesis methods were previously reported [49,50]. The Cu_xS powder was synthesised by photochemical methods using sodium thiosulfate (ACS grade) and copper sulfate (ACS grade) solutions in a weight ratio of 1:1.

The pH was adjusted to 3.0 by adding HNO_3 65% solution; green precipitates were formed in the solution. After 24 h of UV irradiation, the black precipitates were washed and dried at 110 °C for 24 h. The dry Cu_xS powder was calcined at 350 °C in a furnace for 3h. The Cu_xS powder was optimised in our previous papers [49,51]. The FA–TiO_2 composites were obtained by hydrothermal method using 20–40 µm FA fractions and TiO_2 photocatalyst (Degussa P25, 80% anatase, 20% rutile). The FA-TiO_2 composites (Fly1, Fly 2 and respective Fly3) were obtained in an autoclave from the slurry of the powder mixture (weight ratio FA:TiO_2 = 3:1, 1:1 and respective 1:2) and NaOH 2N, under stirring (300 rpm) for 24 h, at 5 atm pressure and 150 °C. After filtration, washing and drying at 105–120 °C, the dried substrates were obtained and further used in photocatalytic and adsorption experiments.

In the preparation process, the FA–TiO_2 and copper sulfide powders were mixed. A schematic diagram was used to explain the preparation method (see Figure 1). Mixing the constituents with ethanol in a weight ratio of 5:1:8, a paste was obtained. The paste was smeared on a microscopy glass substrate (sample of 1.5 × 2.5 cm^2) which was previously cleaned using ethanol, distilled water, and acetone in continuous sonication process. After drying in the air for about 30 min, the films were annealed in an oven at 300 °C for 1 h.

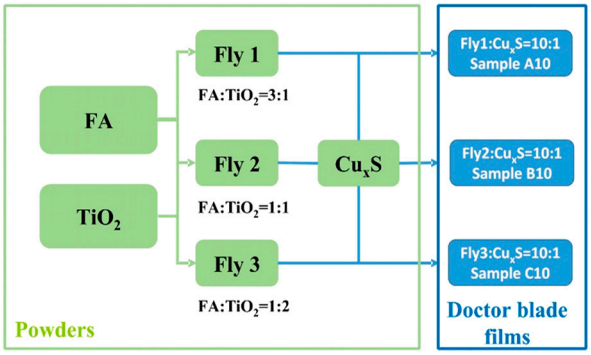

Figure 1. Synthesis of ternary TiO_2–Cu_xS–fly ash (FA) heterostructures.

2.2. Materials Characterisation

The X-ray diffraction (XRD) measurement was used to analyse the phase compositions. The analysis was made at room temperature by using XRD diffraction (Brucker D8 Discover X-ray diffractometer, Berlin, Germany), at 40 kV and 40 mA equipped with a Cu tube for generating CuKα radiation, λ = 0.15406 nm), the incident beam in the 2-Theta mode over the range of 20–70°, scan step of Δθ = 0.025°, and Δt = 1.5 s.

Surface topography, roughness, and fractal distribution of the films were investigated with atomic force microscopy (AFM), (NT-MDT model BL222RNTE). The AFM images were taken in the semicontact mode with Si-tips (NSG10, force constant 0.15 N/m, tip radius 10 nm), and the results were processed with the dedicated software (NT-MDT, Nova Soft). The fractal analysis of the 2D AFM images of the film samples was performed using the SPIP software. Scanning electron microscopy (SEM) (Hitachi model S-3400N Type II) in BSE regime at low vacuum (50 Pa, 15 kV) was used to investigate the morphology of the sample. Energy-dispersive X-ray spectroscopy measurements (EDS) (Thermo, Ultra Dry, Noran System 7, NSS Model, NY, USA) were done for elemental analysis, based on energy values corresponding to each element in the samples.

The point of zero charge of materials (pH_{pzc}) was performed by mass titration using 100 mL 0.1 M NaOH solution, and 0.2 g powder (representative for each sample) was added. In the second step, the solution was titrated with 0.1 M HNO_3 solution, and the pH values measured after 5 min of stirring. The pH of each suspension was then measured using a digital pH meter. Based on the curve obtained after plotting the pH versus mass fraction, the pH_{pzc} was validated. The method was previously developed and explain [49].

2.3. Experimental Setup of Adsorption and Photocatalysis

In order to better understand how simultaneous adsorption and photodegradation processes take place, the experiments were carried out based on the classical photocatalytic degradation models. The methylene blue (MB) degradation measurement was standardised in DIN 52980 as a typical measurement to confirm the photocatalytic activity [52]. The ternary heterostructures, were added in 50 mL of aqueous methylene blue solution (concentration of 4 mg L^{-1}) and irradiated into a photoreactor equipped with two UV blacklight lamps (F18 W/T8 black light tubes, typically 340–400 nm, with λ_{max} = 365 nm, flux intensity 3 lx, Philips, Bucharest, Romania), and four VIS lamps (TL-D Super 80 18 W/865 lamps, white cold light tubes, typically 400–700 nm, with λ_{max} = 565 nm, flux intensity 28 lx, Philips). Before illumination, to ensure the adsorption equilibrium, the heterostructures were kept in the dark in MB solution for 30 min. The adsorption experiments were performed in the same condition in the dark. At given time intervals, 5 mL of the sample was withdrawn and filtered (Millipore Millex-GN 0.2 µm), and the solution absorbance was spectrophotometrically measured at a maximum absorption wavelength of 665 nm (Perkin Elmer Lambda 940 spectrophotometer, Waltham, MA, USA) equipped with a quartz cell. The dye degradation efficiency was calculated as a relative percentage of dye concentration to its initial concentration.

2.4. Adsorption Isotherm Models

The adsorption capacity of MB on ternary materials was calculated using the following expression:

$$q_e = \frac{(C_0 - C_t) \times V}{m} \quad (1)$$

where q_e (mg/g) is the amount adsorbed at time t (minute), and C_0 and C_t (mg/L) are the initial and at time t dye concentrations, respectively. V is the volume of solution (L), and m is the number of adsorbent materials (g).

The equilibrium relationship between dyes adsorbed and many equations described un-adsorbed amounts. Freundlich and Langmuir's models were tested to provide the best description of dye adsorption [53–57].

The Langmuir model predicts whether the adsorption is favourable or unfavourable; the model describes monolayer adsorption to a surface very well. The Langmuir expression and the linearised form are presented in Table 1. A plot of C_e/q_e versus C_e should indicate a straight line of slope $1/q_{max}$ and intercept of $1/K_L \times q_{max}$. A dimensionless constant separation factor (S_F) is the characteristic of Langmuir isotherm, expressed by Equation (2). The value of S_F represents the nature of the adsorption process, which is unfavourable if $S_F > 1$, linear if $S_F = 1$, favourable if $0 < S_F < 1$, and irreversible if $S_F = 0$ [58,59].

$$S_F = \frac{1}{1 + K_L \times C_0} \quad (2)$$

Table 1. The adsorption isotherm models.

Isotherm Models	Math Expression	The Linearised Form	Plots	Parameters
Langmuir	$q_e = \frac{q_{max} \times K_L \times C_e}{1 + K_L \times C_e}$	$\frac{C_e}{q_e} = \frac{1}{K_L \times q_{max}} + \frac{C_e}{q_{max}}$	$\frac{C_e}{q_e}$ vs. C_e	q_{max} = maximum amount of dye per gram of catalyst ($mg \cdot g^{-1}$) K_L = the Langmuir adsorption constant ($L \cdot mg^{-1}$)
Freundlich	$q_e = K_F \times C_e^{1/n}$	$\ln q_e = \ln K_F + \frac{1}{n} \times \ln C_e$	$\ln q_e$ vs. $\ln C_e$	K_F = the Freundlich adsorption constant ($mg \cdot g^{-1}$) n = the Freundlich adsorption constant

C_e = dye concentration at equilibrium ($mg \cdot L^{-1}$), q_e = the adsorbed dye quantity per gram of adsorbent ($mg \cdot g^{-1}$).

The Freundlich model corresponds to a heterogeneous adsorbent surface. The empirical and linearised form of the Freundlich equation can be written as presented in Table 1 [60], where K_F and n are indicators of adsorption capacity and adsorption intensity, respectively. A plot of $\ln(q_e)$ versus $\ln(C_e)$ should indicate a straight line of slope 1/n and intercept $\ln K_F$.

3. Results and Discussion

3.1. Heterostructures Composition and Crystallinity

The ternary heterostructures' composition and crystallinity are considered key properties in developing high efficient photocatalytic and adsorbent materials [61]. The diffraction analysis of Fly ash-TiO_2 structures (named Fly 1, Fly2 and respectively Fly 3) (see Supplementary materials, Figure S1) shows the presence of crystalline oxides such as SiO_2 (monoclinic), Al_2O_3 (hexagonal) and Fe_2O_3 (hematite, rhombohedric) from FA, TiO_2 (anatase, rutile) from Degussa powder, and Cu_2S (chalcocite) and CuS (covellite) from the powder obtained by the photochemical method (Figure 2). Even if the samples were thermally treated at 300 °C, there is no proof of formation of Cu_xO or other mixed oxides. However, due to the similarity of the metal ionic radius ($r_{Al^{3+}} = 0.050$ nm, $r_{Fe^{3+}} = 0.06$ nm, $r_{Ti^{4+}} = 0.068$ nm, and $r_{Cu^{2+}} = 0.072$ nm), the doping between heterostructure materials cannot be excluded. Materials compatibility is a pre-requisite in obtaining uniform and homogeneous interfaces that can facilitate the charge carrier's mobility through the structure.

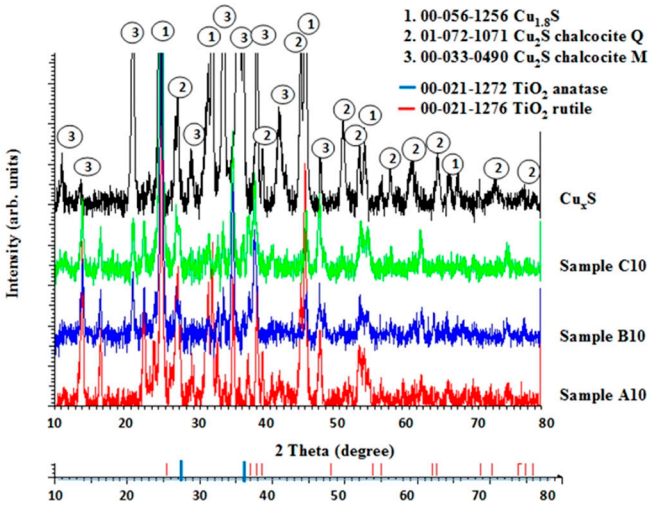

Figure 2. X-ray diffraction (XRD) patterns for ternary TiO_2–Cu_xS–FA heterostructures.

Energy-dispersive X-ray spectroscopy (EDS) technique was employed to get information about the elemental composition of the ternary TiO_2–Cu_xS–FA structures. The percentage weight and atomic content of various elements of the surface determined by EDS are shown in Table 2. This information is essential, considering that photocatalysis and adsorption processes are dependent on surface chemistry [62]. Based on the EDS results, titanium oxide is the most surface-abundant, which is a positive aspect due to the well-known photocatalytic efficiency of this material [63]. Additionally, the sample's surface contains all components required for heterostructure activation in UV radiation. Sample C10 is the most suitable zeolite material because the Si/Al ratio is 2.60, which is closest to the value recommended in the literature of 2.10 [64,65].

Table 2. The weight and atomic percentage of each element in ternary TiO_2–CuxS–FA materials (from Energy-dispersive X-ray spectroscopy (EDS) spectra).

Sample	Line	O K	Na K	Al K	Si K	S K	Ti K	Fe K	Cu K	Total	Si:Al	Ti:Cu:Si
A10	Wt. %	41.66	8.69	7.78	12.69	1.36	20.04	2.81	4.97	100		
	At. %	60.39	8.77	6.69	10.48	0.99	9.70	1.17	1.81	100	1.57	5.35:1:5.79
B10	Wt. %	40.80	6.09	4.52	7.81	0.71	34.71	2.77	2.60	100		
	At. %	62.23	6.47	4.09	6.78	0.54	17.68	1.21	1.00	100	1.66	17.68:1:6.78
C10	Wt. %	41.95	4.30	3.67	9.94	1.19	34.64	1.29	0.56	100		
	At. %	63.48	4.53	3.30	8.57	0.90	17.51	3.02	1.15	100	2.60	15.22:1:7.5

3.2. Heterostructures Morphology and Point of Zero Charge (pH_{PZC})

The morphology is an important property that can influence both photocatalytic efficiency and adsorption that take place at the heterostructure's interface with the working environment. The AFM images presented in Figure 3 show that meso- and micro-particles are agglomerated in large aggregates depending on the heterostructure composition.

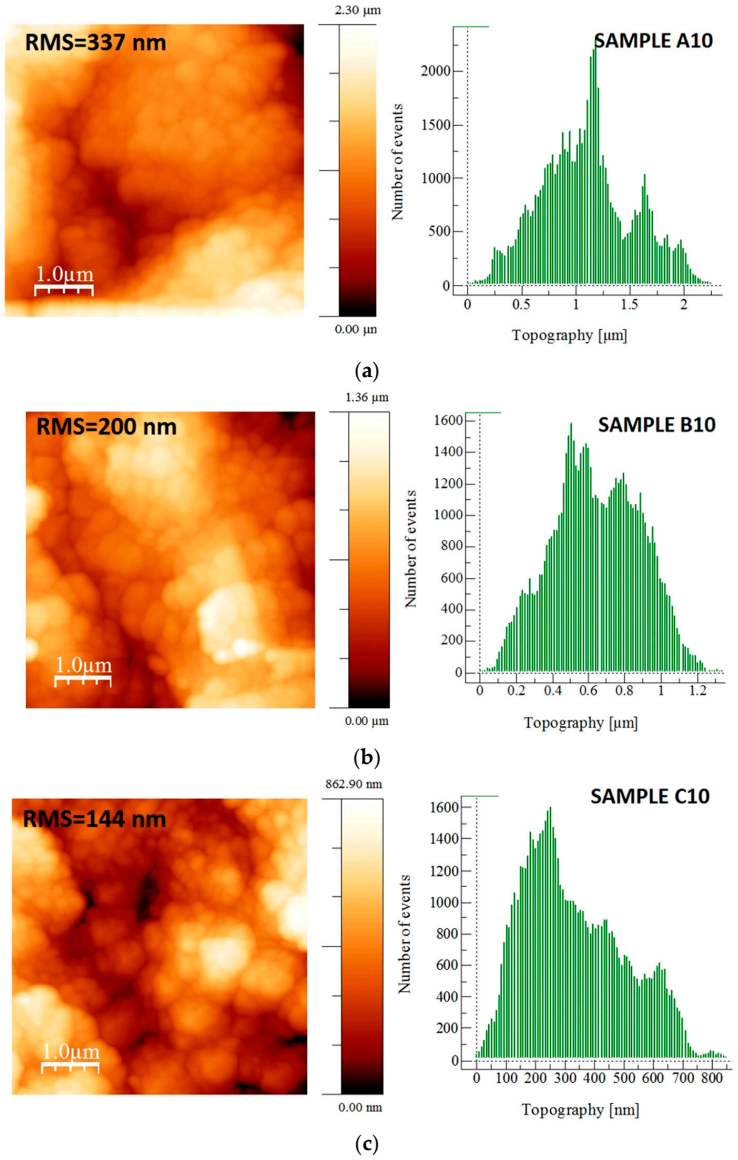

Figure 3. The AFM images and distribution curves of ternary heterostructures: (**a**) sample A10, (**b**) sample B10, (**c**) sample C10.

Sample A10 presented a porous morphology with an average pore size around 1 µm (Figure 3a), which is considered suitable for photocatalytic application due to the scattering effect [49]. By decreasing the FA quantity and increasing the TiO_2 ratio, the pore size value decreases significantly (~600 nm for sample B10, see Figure 3b, and ~250 nm for sample C10, see Figure 3c); even if the size of the pores decreases, the number of pores increases, which is in accordance with other reports [66], suggesting the possibility of tailoring the morphology based on the heterostructure components ratio.

The Scanning electron microscopy (SEM) images (see Figure 4) indicate that all three samples contain aggregates of various shape and size un-homogenously distributed on the surface. This morphology is characteristic for ternary heterostructures [65] where metal oxides or sulfur compounds (TiO_2, Cu_2S) adhere to the fly ash particle surfaces. Most of the particles have a spherical shape, with sizes ranging from 200 to 500 nm dispersed over the whole matrix of materials. By maximising the surface area, it is possible to increase the photocatalytic efficiency due to the larger interface between the samples and the aqueous environment.

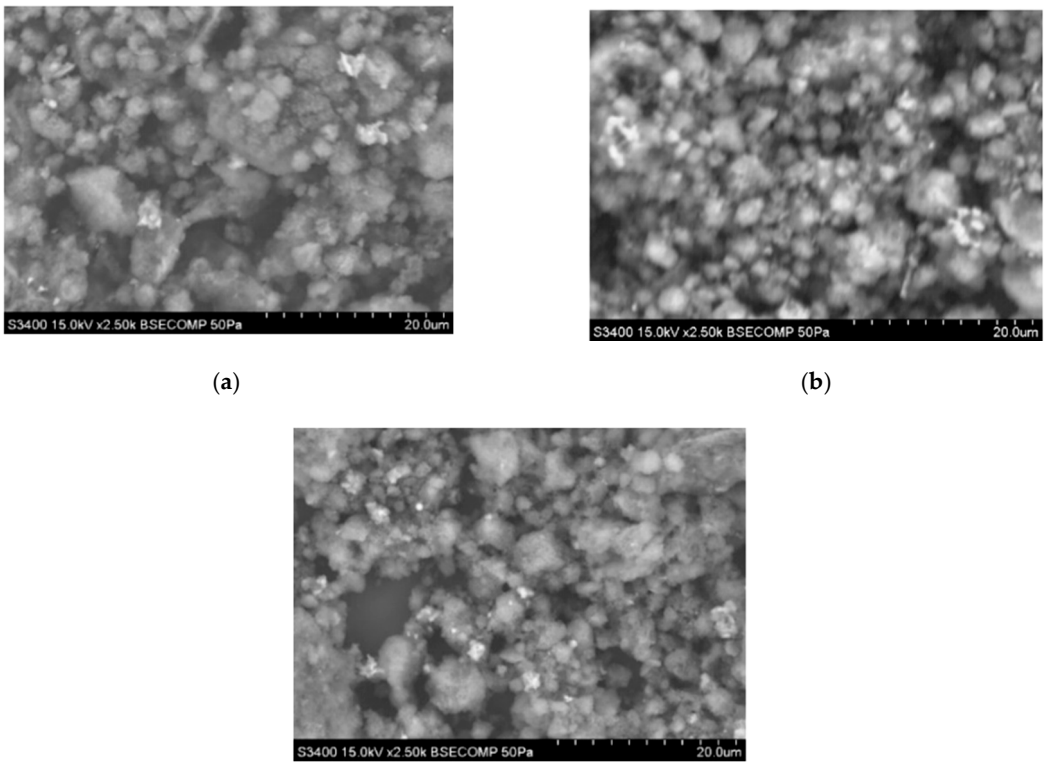

(**a**) (**b**)

(**c**)

Figure 4. SEM images of ternary TiO_2–CuxS–FA heterostructures: (**a**) Sample A10, (**b**) Sample B10, (**c**) Sample C10.

Suitable charged surfaces and porous morphologies are considered prerequisites for high efficient photocatalytic and adsorption processes [67]. The photocatalysis and adsorption reaction on the nanostructures materials are influenced by a few factors: (i) the pH of the pollutant, (ii) the ionizing capacity of the solute (acidity, pKa), and (iii) the zero point charge of materials (pH_{PZC}). The values of pH_{PZC} calculated based on Figure 5, i.e., 6.43 for sample A10, 6.32 for Sample B10 and 6.25 for Sample C10, indicated an amphoteric surface of nanostructures favourable for adsorption and photocatalysis.

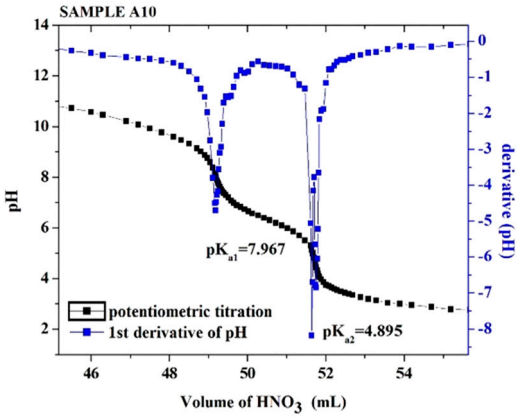

(**a**)

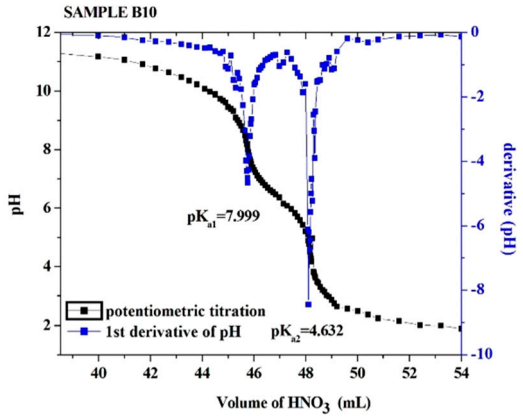

(**b**)

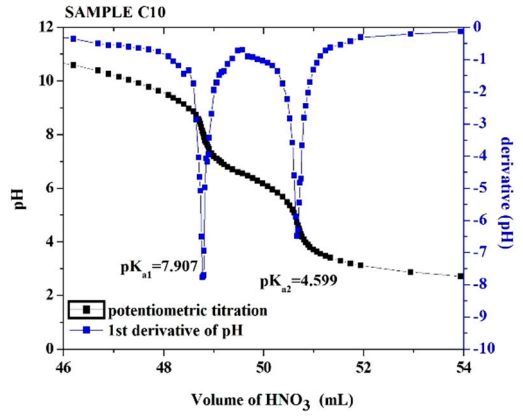

(**c**)

Figure 5. pH changes in the photocatalyst films vs. total HNO_3 0.1M volume (black line) and the derivative curve (dpH/dV, blue line), (**a**). sample A10, (**b**). sample B10, (**c**). sample C10.

3.3. Adsorption and Photocatalytic Processes

Heterogeneous photocatalytic processes comprise several steps, such as physical [51] or chemical [68] adsorption, chemical reactions occurring between the species formed at the catalyst surface followed by degradation and reaction products formation (such as halides, metals, inorganic acids, organic compounds), and adsorption/desorption of these products. Therefore, the description of heterogeneous photocatalysis with specific adsorption modelling tools also involves the consideration of secondary chemical processes (pseudo-adsorption) [69], to which is added the influence of substrate morphology, especially in the inter-particle diffusion stage.

Since the adsorption step determines the rate in heterogeneous photocatalytic processes, its study becomes necessary for understanding the photodegradation mechanism. The adsorption mechanism involved four steps: (a) surface pollutant diffusion, (b) the mass transfer between the substrate and liquid phase, (c) catalyst surface pollutant adsorption, and (d) adsorbed molecules diffusion through catalyst pores [70–72].

Due to the strong adsorption of dye molecules on the ternary heterostructure surface, the photocatalysis process takes place at a considerable rate higher than Fly ash-TiO_2 materials (see in the Suplementary material Figure S2 for adsorption process and Figure S3 for adsorption/photocatalysis process). MB adsorption was firstly conducted in a dark condition (see Figure 6), followed by its photocatalytic degradation with and without the addition of H_2O_2 under UV irradiation (see Figure 7).

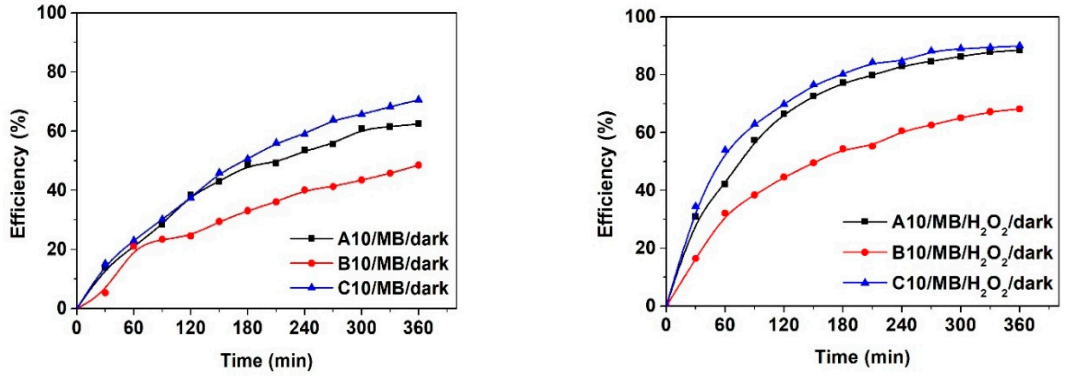

Figure 6. The adsorption process on ternary TiO_2–Cu_xS–FA materials: (**a**) without H_2O_2 and (**b**) with H_2O_2.

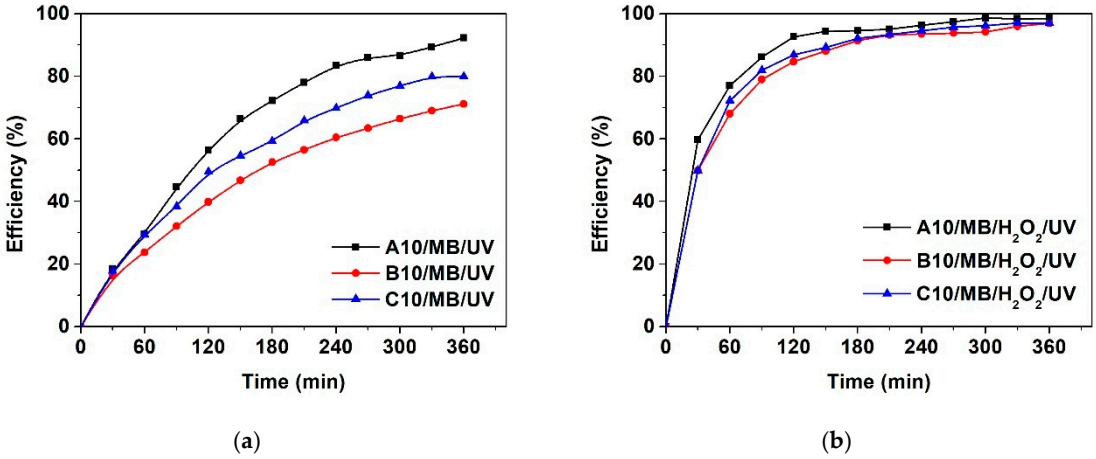

Figure 7. The adsorption/photocatalysis process on ternary TiO_2–Cu_xS–FA materials: (**a**) without H_2O_2 and (**b**) with H_2O_2.

The adsorption behaviour can serve as an essential role in the photocatalytic degradation reaction. The need for kinetic investigations in heterogeneous photocatalysis is closely related to the photoreactor design as well as the choice of that reaction mechanism sequence with a determining effect on the photoreactor performance. The highest adsorption efficiency (in the dark) was 75% (without H_2O_2) and 90% (with H_2O_2), both corresponding to sample C10 due to its morphology, characterised by a high number of small pores. Under UV irradiation, the sample A10 becomes more efficient (96% without H_2O_2 and 99% with H_2O_2) due to the higher TiO_2 content and the presence of larger pores allowing a multi-scattering effect [73].

Sample A10 have a better suppression of the electron-hole recombination, which allows the generation of oxidative species (h^+, HO·) [74]. It is known that fast electron-hole pairs recombination correlated with lacking efficient export channels induce a significant reduction of the photocatalytic efficiency [75,76]. The superoxide radicals (HO·) generated in the presence of surface holes (h^+) present a strong ability of oxidative degradation and are used as active species in MB degradation reaction. Based on the present experimental results which consider satisfactory photocatalytic degradation activity and good charge separation, the ternary heterostructure can be further tested in dynamic system applications.

The superoxide radicals (HO) generated in the presence of surface holes (h^+) present a strong oxidative degradation ability and are used as active species in MB degradation reaction. Based on the present experimental results, which consider satisfactory photocatalytic degradation activity and good charge separation, the ternary heterostructure can be further tested in dynamic system applications.

The main oxides present in fly ash are mullite ($2SiO_2 \cdot 3Al_2O_3$), α-quartz (SiO_2), hematite (α-Fe_2O_3), and magnetite (Fe_3O_4), which comprise over 70% of the fly ash. The majority of oxides present in fly ash are photocatalytic inactive; fly ash is a good adsorbent in dye removal. The magnetite and hematite, together with hydrogen peroxide, act as in situ Fenton reactive, which improves the efficiency of dyes degradation. The results presented in Figures 6b and 7b demonstrate that in situ Fenton and photo-Fenton homogeneous processes, caused by the Fe^{2+}, Mn^{3+} and Cu^{2+}, on the surface of the fly-ash-based material increase the MB degradation very quickly. Under UV irradiation, the effect of H_2O_2 is much stronger, and the efficiency strongly increases, suggesting these materials be recommended for wastewater remediation.

Fenton is a homogeneous process that consists of ferrous, cuprous and cupric ions and hydrogen peroxide reaction that generated hydroxyl radical as in Equations (3)–(5) [77,78]. The hydroxyl radicals degrade dye molecules, resulting in intermediates and mineralisation products as in Equation (6).

$$Fe^{2+} + H_2O_2 \rightarrow Fe^{3+} + OH^- + HO^{\cdot} \quad (3)$$

$$Cu^{2+} + H_2O_2 \rightarrow Cu^{+} + HO_2^{\cdot} + H^+ \quad (4)$$

$$Cu^{+} + H_2O_2 \rightarrow Cu^{2+} + HO^{\cdot} + HO^- \quad (5)$$

$$HO^{\cdot} + \text{dyes} \rightarrow \text{intermediates} \rightarrow \text{inorganics} \quad (6)$$

The heterojunctions are used for photocatalyst due to their carrier-injecting-ratio properties, improving the light response and achieving more efficient separation of photoexcited electron-hole pairs and thus achieving a higher photocatalytic reaction rate and overall output. These hybrid materials consist of a wide range of oxides from fly ash (SiO_2, Al_2O_3, Fe_2O_3), TiO_2 Degussa P25, and copper sulfides (CuS, Cu_2S); will take advantage of the very stable TiO_2 photocatalyst; and, coupled with the VIS response of the copper sulphide (Cu_xS, $1 < x < 2$) photocatalyst, will yield a hybrid photocatalyst which provides excellent photocatalytic performance in visible light and cost-effectiveness [79].

3.4. Adsorption Isotherms

Two isotherm models, Langmuir and Freundlich, are often used to determine the maximum pollutant capacity and to identify the adsorption process, the data were fitted to match the experimental data. The isotherm parameters and the values of the correlation coefficients (R^2) are summarised in Table 3.

Table 3. Isotherm data for the adsorption of methylene blue (MB) on the ternary heterostructures (TiO_2–Cu_xS–FA) and TiO_2:FA composites.

Adsorbat	Adsorbent System	Langmuir Adsorption Isotherm				Freundlich Adsorption Isotherm		
		q_{max} (mg/g)	K_L (L/mg)	Correlation Coefficient (R^2)	Separation Factor (S_F)	(1/n)	K_F (mg/g)/(mg/L)	R^2
TiO_2:FA	Fly 1	0.34316	0.95091	0.81714	0.20859	1.008	1.752	0.84752
	Fly1/H_2O_2	0.61348	1.64123	0.93782	0.13248	1.551	1.488	0.93372
	Fly 2	0.36597	8.31400	0.96815	0.02926	0.805	1.502	0.97459
	Fly2/H_2O_2	0.46289	5.31114	0.87451	0.04506	1.426	3.464	0.81278
	Fly 3	0.39512	1.10957	0.85531	0.18426	1.113	2.543	0.88178
	Fly3/H_2O_2	0.43805	0.90199	0.87311	0.21744	1.272	2.456	0.87442
Sample A10	Fly1-Cu_xS	0.29346	0.76514	0.89664	0.24674	0.746	1.906	0.92464
	Fly1-Cu_xS/H_2O_2	0.79888	2.75445	0.94830	0.08340	2.458	3.824	0.88054
Sample B10	Fly2-Cu_xS	0.21061	2.19786	0.95273	0.10236	0.516	2.016	0.97168
	Fly2-Cu_xS/H_2O_2	0.47047	0.44766	0.94939	0.35892	1.071	6.958	0.95102
Sample C10	Fly3-Cu_xS	0.36371	1.20442	0.90034	0.17225	0.928	2.196	0.9175
	Fly3-Cu_xS/H_2O_2	1.02334	0.35541	0.97737	0.41355	3.303	2.939	0.91938

The adsorption equilibrium data fit the Langmuir isotherm. The results show that the value of R^2 obtained from both isotherms was in the range of 0.817 and 0.977, assuming that the adsorption of MB is monolayered chemisorption. The maximum monolayer adsorption capacity was 1 $mg \cdot g^{-1}$ for sample C10 when H_2O_2 was used. The separation factor S_F was in the range of 0.029 and 0.413 for all samples, showing that the adsorption of MB on fly ash-TiO_2 based materials is favourable. The adsorption mechanism of MB on ternary materials surface can be explained to the electrostatic interaction between negative charge of materials and positively charge of dye, showing that the process is chemisorption.

The constants of the Freundlich model, K_F and 1/n ranged from 1.488 to 6.958 and from 0.516 to 3.3, respectively. If 1/n has a value between 0 and 1, then the adsorption is favourable. The MB adsorption on the A10, B10, and C10 samples were favourable in the absence of H_2O_2. The high correlation coefficients values of Freundlich model from 0.81 to 0.977 indicate a high affinity between the materials surface and MB. These results indicated that some heterogeneity in the surface of the materials plays a role in the adsorption process, which is in agreement with the presence of both Cu_xS and TiO_2 in the adsorbent structure.

4. Conclusions

Fly ash is a solid waste generated in the combustion of coal. A strategy proposed to prevent environmental pollution is to use FA in wastewater environmentally friendly applications, such as photocatalysis. The majority of raw FA consists of numerous metal oxides such as silica (SiO_2), alumina (Al_2O_3), calcium oxide (CaO), magnesium oxide (MgO), iron oxide (Fe_2O_3), and titania (TiO_2) with good photocatalytic activity. In this work, considering the intelligent management of fly ash, this raw material was used in ternary TiO_2–Cu_xS–FA heterostructure with application in advanced wastewater treatment. The TiO_2–Cu_xS–FA heterostructures give the possibility to get simultaneous adsorption and photocatalytic unit operations in a single reactor. The modelling of such a system must adequately take into account the dual functionality of materials, to set linking between adsorption and photodegradation mechanisms. The comparison between the adsorption and photodegradation tests performed with TiO_2–Cu_xS–FA with different TiO_2 ratios showed that in dark conditions, the methylene blue removal was 75% after 360 min, while in the presence of UV light, the efficiency was 96% after the same treatment period. The degradation rate of MB, when H_2O_2 is used as an electron acceptor, could reach 90% in adsorption and 99% in combined adsorption/photocatalysis processes. The adsorption isotherm was found to follow the Langmuir and Freundlich models.

Supplementary Materials: The following are available online at http://www.mdpi.com/2076-3417/10/22/8070/s1, Figure S1: The XRD pattern of Fly ash-TiO_2 materials: Fly1 (black), Fly2 (red) and Fly 3 (blue), Figure S2: The adsorption process on Fly ash-TiO_2 materials: (**a**) without H_2O_2 and (**b**) with H_2O_2, Figure S3: The adsorption/photocatalysis process on Fly ash-TiO_2 materials: (**a**) without H_2O_2 and (**b**) with H_2O_2.

Author Contributions: Conceptualisation, L.A.; methodology, L.I.; validation, C.C., L.A., and L.I.; formal analysis, A.E.; investigation, L.I.; resources, C.C.; data curation, L.I.; writing—original draft preparation, review and editing, L.A.; writing, A.E.; visualisation, C.C.; project administration, L.A. All authors have read and agreed to the published version of the manuscript.

Funding: This research received no external funding.

Conflicts of Interest: The authors declare no conflict of interest.

References

1. Rathnayake, M.; Julnipitawong, P.; Tangtermsirikul, S.; Toochinda, P. Utilization of Coal Fly Ash and Bottom Ash as Solid Sorbents for Sulfur Dioxide Reduction from Coal Fired Power Plant: Life Cycle Assessment and Applications. *J. Clean. Prod.* **2018**, *202*, 934–945. [CrossRef]
2. Kurda, R.; de Brito, J.; Silvestre, J.D. Water Absorption and Electrical Resistivity of Concrete with Recycled Concrete Aggregates and Fly Ash. *Cem. Concr. Compos.* **2019**, *95*, 169–182. [CrossRef]
3. Zhao, M.; Yuan, Q.; Zhang, H.; Li, C.; Wang, Y.; Wang, W. Synergy of Adsorption and Photocatalysis on Removal of High-Concentration Dye by Ag/AgCl/$Bi_6O_4(OH)_4(NO_3)_6{\cdot}H_2O$ Nanocomposite Using $Bi_{12}O_{17}C_{l2}$ as Bismuth Source. *J. Alloys Compd.* **2019**, *782*, 1049–1057. [CrossRef]
4. Liu, X.W.; Shen, L.Y.; Hu, Y.H. Preparation of TiO_2-Graphene Composite by a Two-Step Solvothermal Method and Its Adsorption-Photocatalysis Property. *Water Air Soil Pollut.* **2016**, *227*, 141. [CrossRef]
5. Sacco, O.; Matarangolo, M.; Vaiano, V.; Libralato, G.; Guida, M.; Lofrano, G.; Carotenuto, M. Crystal Violet and Toxicity Removal by Adsorption and Simultaneous Photocatalysis in a Continuous Flow Micro-Reactor. *Sci. Total Environ.* **2018**, *644*, 430–438. [CrossRef] [PubMed]
6. Long, Y.; Huang, D.; Luo, L.; Li, L.; Wang, L.; Zhang, S.; Jiang, F. Enhanced Degradation of 17β-Estradiol by AgI/N-Bi_2O_3 Composite: Strong Synergy of Adsorption–Photocatalysis. *Res. Chem. Intermed.* **2018**, *44*, 7117–7133. [CrossRef]
7. Zhang, F.; Yang, C.; Wang, X.-X.; Li, R.; Wan, Z.; Wang, X.; Wan, Y.; Long, Y.-Z.; Cai, Z. Graphene Quantum Dots Doped PVDF(TBT)/PVP(TBT) Fiber Film with Enhanced Photocatalytic Performance. *Appl. Sci.* **2020**, *10*, 596. [CrossRef]
8. Bai, S.; Gao, C.; Low, J.; Xiong, Y. Crystal Phase Engineering on Photocatalytic Materials for Energy and Environmental Applications. *Nano Res.* **2019**, *12*, 2031–2054. [CrossRef]
9. Al-Mamun, M.R.; Kader, S.; Islam, M.S.; Khan, M.Z.H. Photocatalytic Activity Improvement and Application of UV-TiO_2 Photocatalysis in Textile Wastewater Treatment: A Review. *J. Environ. Chem. Eng.* **2019**, *7*, 103248. [CrossRef]
10. Smazna, D.; Shree, S.; Polonskyi, O.; Lamaka, S.; Baum, M.; Zheludkevich, M.; Faupel, F.; Adelung, R.; Mishra, Y.K. Mutual Interplay of ZnO Micro-and Nanowires and Methylene Blue during Cyclic Photocatalysis Process. *J. Environ. Chem. Eng.* **2019**, *7*, 103016. [CrossRef]
11. Karunakaran, C.; Vinayagamoorthy, P. Perforated $ZnFe_2O_4$/ZnO Hybrid Nanosheets: Enhanced Charge-Carrier Lifetime, Photocatalysis, and Bacteria Inactivation. *Appl. Phys. A* **2017**, *123*, 472. [CrossRef]
12. Enesca, A.; Andronic, L.; Duta, A. Optimization of Opto-Electrical and Photocatalytic Properties of SnO2 Thin Films Using Zn^{2+} and W^{6+} Dopant Ions. *Catal. Lett.* **2012**, *142*, 224–230. [CrossRef]
13. Huy, T.H.; Bui, D.P.; Kang, F.; Wang, Y.-F.; Liu, S.-H.; Thi, C.M.; You, S.-J.; Chang, G.-M.; Pham, V.V. SnO_2/TiO_2 Nanotube Heterojunction: The First Investigation of NO Degradation by Visible Light-Driven Photocatalysis. *Chemosphere* **2019**, *215*, 323–332. [CrossRef] [PubMed]
14. Enesca, A.; Andronic, L.; Duta, A. The Influence of Surfactants on the Crystalline Structure, Electrical and Photocatalytic Properties of Hybrid Multi-Structured (SnO_2, TiO_2 and WO_3) Thin Films. *Appl. Surf. Sci.* **2012**, *258*, 4339–4346. [CrossRef]
15. Tahir, M.B.; Nabi, G.; Rafique, M.; Khalid, N.R. Nanostructured-Based WO_3 Photocatalysts: Recent Development, Activity Enhancement, Perspectives and Applications for Wastewater Treatment. *Int. J. Environ. Sci. Technol.* **2017**, *14*, 2519–2542. [CrossRef]

16. Xie, X.; Li, Y.; Yang, Y.; Chen, C.; Zhang, Q. UV–Vis–IR Driven Thermocatalytic Activity of OMS_2/SnO_2 Nanocomposite Significantly Enhanced by Novel Photoactivation and Synergetic Photocatalysis-Thermocatalysis. *Appl. Surf. Sci.* **2018**, *462*, 590–597. [CrossRef]
17. Praus, P.; Svoboda, L.; Dvorský, R.; Reli, M. Nanocomposites of SnO_2 and G-C_3N_4: Preparation, Characterization and Photocatalysis under Visible LED Irradiation. *Ceram. Int.* **2018**, *44*, 3837–3846. [CrossRef]
18. Gu, J.; Zang, H.; Yao, S.; Wang, X.; Zhu, M.; Song, H. Study on Degradation of Benzothiazolium-Based Ionic Liquids by UV-H_2O_2. *Appl. Sci.* **2020**, *10*, 894. [CrossRef]
19. Kalikeri, S.; Shetty Kodialbail, V. Solar Light-Driven Photocatalysis Using Mixed-Phase Bismuth Ferrite ($BiFeO_3/Bi_{25}FeO_{40}$) Nanoparticles for Remediation of Dye-Contaminated Water: Kinetics and Comparison with Artificial UV and Visible Light-Mediated Photocatalysis. *Environ. Sci. Pollut. Res.* **2018**, *25*, 13881–13893. [CrossRef]
20. Robert, D.; Keller, N.; Selli, E. Environmental Photocatalysis and Photochemistry for a Sustainable World: A Big Challenge. *Environ. Sci. Pollut. Res.* **2017**, *24*, 12503–12505. [CrossRef]
21. Alshehri, M.; Al-Marzouki, F.; Alshehrie, A.; Hafez, M. Synthesis, Characterization and Band Alignment Characteristics of NiO/SnO_2 Bulk Heterojunction Nanoarchitecture for Promising Photocatalysis Applications. *J. Alloys Compd.* **2018**, *757*, 161–168. [CrossRef]
22. Sivaranjani, R.; Thayumanavan, A.; Sriram, S. Photocatalytic Activity of Zn-Doped Fe_2O_3 Nanoparticles: A Combined Experimental and Theoretical Study. *Bull. Mater. Sci.* **2019**, *42*, 185. [CrossRef]
23. Enesca, A.; Yamaguchi, Y.; Terashima, C.; Fujishima, A.; Nakata, K.; Duta, A. Enhanced UV–Vis Photocatalytic Performance of the $CuInS_2/TiO_2/SnO_2$ Hetero-Structure for Air Decontamination. *J. Catal.* **2017**, *350*, 174–181. [CrossRef]
24. Wang, Z.; Song, G.; Xu, J.; Fu, Q.; Pan, C. Electrospun Titania Fibers by Incorporating Graphene/Ag Hybrids for the Improved Visible-Light Photocatalysis. *Front. Mater. Sci.* **2018**, *12*, 379–391. [CrossRef]
25. 2Cui, L.; Meng, X.; Fan, Y.; Li, X.; Bi, C. Synthesis, Crystal Structures, Photocatalysis for Rhodamine B Degradation of a Organobismuth (V) Dithiocarbamate Polymer [$PhBiS_2CN(C_2H_5)2Cl$]N. *J. Inorg. Organomet. Polym. Mater.* **2015**, *25*, 1490–1494.
26. Enesca, A.; Andronic, L.; Duta, A. Wastewater Treatment Using Optimized TiO_2 Photocatalytic Properties. *Environ. Eng. Manag. J.* **2009**, *8*, 753–758. [CrossRef]
27. Baneto, M.; Enesca, A.; Mihoreanu, C.; Lare, Y.; Jondo, K.; Napo, K.; Duta, A. Effects of the Growth Temperature on the Properties of Spray Deposited $CuInS_2$ Thin Films for Photovoltaic Applications. *Ceram. Int.* **2015**, *41*, 4742–4749. [CrossRef]
28. Grilla, E.; Matthaiou, V.; Frontistis, Z.; Oller, I.; Polo, I.; Malato, S.; Mantzavinos, D. Degradation of Antibiotic Trimethoprim by the Combined Action of Sunlight, TiO_2 and Persulfate: A Pilot Plant Study. *Catal. Today* **2019**, *328*, 216–222. [CrossRef]
29. Davies, C.M.; Roser, D.J.; Feitz, A.J.; Ashbolt, N.J. Solar Radiation Disinfection of Drinking Water at Temperate Latitudes: Inactivation Rates for an Optimised Reactor Configuration. *Water Res.* **2009**, *43*, 643–652. [CrossRef]
30. Fujishima, A.; Zhang, X.; Tryk, D. Heterogeneous Photocatalysis: From Water Photolysis to Applications in Environmental Cleanup. *Int. J. Hydrog. Energy* **2007**, *32*, 2664–2672. [CrossRef]
31. Nakata, K.; Fujishima, A. TiO_2 Photocatalysis: Design and Applications. *J. Photochem. Photobiol. C Photochem. Rev.* **2012**, *13*, 169–189. [CrossRef]
32. Georgieva, J.; Valova, E.; Armyanov, S.; Philippidis, N.; Poulios, I.; Sotiropoulos, S. Bi-Component Semiconductor Oxide Photoanodes for the Photoelectrocatalytic Oxidation of Organic Solutes and Vapours: A Short Review with Emphasis to TiO_2–WO_3 Photoanodes. *J. Hazard. Mater.* **2012**, *211–212*, 30–46. [CrossRef] [PubMed]
33. Lu, Y.; Yi, G.; Jia, J.; Liang, Y. Preparation and Characterization of Patterned Copper Sulfide Thin Films on N-Type TiO_2 Film Surfaces. *Appl. Surf. Sci.* **2010**, *256*, 7316–7322. [CrossRef]
34. Chen, S.; Zhao, W.; Liu, W.; Zhang, S. Preparation, Characterization and Activity Evaluation of p–n Junction Photocatalyst p-ZnO/n-TiO_2. *Appl. Surf. Sci.* **2008**, *255*, 2478–2484. [CrossRef]
35. Bayati, M.R.; Golestani-Fard, F.; Moshfegh, A.Z.; Molaei, R. A Photocatalytic Approach in Micro Arc Oxidation of WO_3–TiO_2 Nano Porous Semiconductors under Pulse Current. *Mater. Chem. Phys.* **2011**, *128*, 427–432. [CrossRef]

36. Belessi, V.; Lambropoulou, D.; Konstantinou, I.; Zboril, R.; Tucek, J.; Jancik, D.; Albanis, T.; Petridis, D. Structure and Photocatalytic Performance of Magnetically Separable Titania Photocatalysts for the Degradation of Propachlor. *Appl. Catal. B Environ.* **2009**, *87*, 181–189. [CrossRef]
37. Yuan, J.; Zhang, X.; Li, H.; Wang, K.; Gao, S.; Yin, Z.; Yu, H.; Zhu, X.; Xiong, Z.; Xie, Y. TiO_2/SnO_2 Double-Shelled Hollow Spheres-Highly Efficient Photocatalyst for the Degradation of Rhodamine B. *Catal. Commun.* **2015**, *60*, 129–133. [CrossRef]
38. Wang, M.; Ju, P.; Li, J.; Zhao, Y.; Han, X.; Hao, Z. Facile Synthesis of MoS_2/g-C_3N_4/GO Ternary Heterojunction with Enhanced Photocatalytic Activity for Water Splitting. *ACS Sustain. Chem. Eng.* **2017**, *5*, 7878–7886. [CrossRef]
39. Raghavan, N.; Thangavel, S.; Venugopal, G. Enhanced Photocatalytic Degradation of Methylene Blue by Reduced Graphene-Oxide/Titanium Dioxide/Zinc Oxide Ternary Nanocomposites. *Mater. Sci. Semicond. Process.* **2015**, *30*, 321–329. [CrossRef]
40. Zhao, H.; Wu, M.; Liu, J.; Deng, Z.; Li, Y.; Su, B.-L. Synergistic Promotion of Solar-Driven H_2 Generation by Three-Dimensionally Ordered Macroporous Structured TiO_2-Au-CdS Ternary Photocatalyst. *Appl. Catal. B Environ.* **2016**, *184*, 182–190. [CrossRef]
41. Ma, P.; Jiang, W.; Wang, F.; Li, F.; Shen, P.; Chen, M.; Wang, Y.; Liu, J.; Li, P. Synthesis and Photocatalytic Property of Fe_3O_4@TiO_2 Core/Shell Nanoparticles Supported by Reduced Graphene Oxide Sheets. *J. Alloys Compd.* **2013**, *578*, 501–506. [CrossRef]
42. Hou, H.; Gao, F.; Wang, L.; Shang, M.; Yang, Z.; Zheng, J.; Yang, W. Superior Thoroughly Mesoporous Ternary Hybrid Photocatalysts of TiO_2/WO_3/g-C_3N_4 Nanofibers for Visible-Light-Driven Hydrogen Evolution. *J. Mater. Chem. A* **2016**, *4*, 6276–6281. [CrossRef]
43. Li, Z.D.; Wang, H.L.; Wei, X.N.; Liu, X.Y.; Yang, Y.F.; Jiang, W.F. Preparation and Photocatalytic Performance of Magnetic Fe_3O_4@TiO_2 Core-Shell Microspheres Supported by Silica Aerogels from Industrial Fly Ash. *J. Alloys Compd.* **2016**, *659*, 240–247. [CrossRef]
44. Liu, S.; Zhu, J.; Guo, X.; Ge, J.; Wu, H. Preparation of α-Fe_2O_3-TiO_2/Fly Ash Cenospheres Photocatalyst and Its Mechanism of Photocatalytic Degradation. *Colloids Surfaces A Physicochem. Eng. Asp.* **2015**, *484*, 434–440. [CrossRef]
45. Liu, S.; Zhu, J.; Yang, Q.; Xu, P.; Ge, J.; Guo, X. Preparation of SnO_2-TiO_2/Fly Ash Cenospheres and Its Application in Phenol Degradation. *Photochem. Photobiol.* **2015**, *91*, 1302–1308. [CrossRef]
46. Zhao, Z.; Lei, Y.; Liu, W.; Fan, J.; Xue, D.; Xue, Y.; Yin, S. Fly Ash Cenospheres as Multifunctional Supports of G-C_3N_4/N-TiO_2 with Enhanced Visible-Light Photocatalytic Activity and Adsorption. *Adv. Powder Technol.* **2017**, *28*, 3233–3240. [CrossRef]
47. Kanakaraju, D.; bin Ya, M.H.; Lim, Y.-C.; Pace, A. Combined Adsorption/Photocatalytic Dye Removal by Copper-Titania-Fly Ash Composite. *Surf. Interfaces* **2020**, *19*, 100534. [CrossRef]
48. Visa, M.; Chelaru, A.-M. Hydrothermally Modified Fly Ash for Heavy Metals and Dyes Removal in Advanced Wastewater Treatment. *Appl. Surf. Sci.* **2014**, *303*, 14–22. [CrossRef]
49. Andronic, L.; Isac, L.; Miralles-Cuevas, S.; Visa, M.; Oller, I.; Duta, A.; Malato, S. Pilot-Plant Evaluation of TiO_2 and TiO_2-Based Hybrid Photocatalysts for Solar Treatment of Polluted Water. *J. Hazard. Mater.* **2016**, *320*, 469–478. [CrossRef]
50. Visa, M.; Andronic, L.; Duta, A. Fly Ash-TiO_2 Nanocomposite Material for Multi-Pollutants Wastewater Treatment. *J. Environ. Manage.* **2015**, *150*, 336–343. [CrossRef]
51. Andronic, L.; Isac, L.; Duta, A. Photochemical Synthesis of Copper Sulphide/Titanium Oxide Photocatalyst. *J. Photochem. Photobiol. A Chem.* **2011**, *221*, 30–37. [CrossRef]
52. German Standard No. 52980. Photocatalytic Activity Of Surfaces-Determination Of Photocatalytic Activity By Degradation Of Methylene Blue. *Ger. Inst. Stand. (Deutsches Inst. für Normung)* **2008**, *10*, 1–14.
53. Ahmaruzzaman, M. A Review on the Utilization of Fly Ash. *Prog. Energy Combust. Sci.* **2010**, *36*, 327–363. [CrossRef]
54. Mall, I.D.; Srivastava, V.C.; Agarwal, N.K. Removal of Orange-G and Methyl Violet Dyes by Adsorption onto Bagasse Fly Ash-Kinetic Study and Equilibrium Isotherm Analyses. *Dye. Pigment.* **2006**, *63*, 210–223. [CrossRef]
55. Sun, D.; Zhang, X.; Wu, Y.; Liu, X. Adsorption of Anionic Dyes from Aqueous Solution on Fly Ash. *J. Hazard. Mater.* **2010**, *181*, 335–342. [CrossRef]

56. Dizge, N.; Aydiner, C.; Demirbas, E.; Kobya, M.; Kara, S. Adsorption of Reactive Dyes from Aqueous Solutions by Fly Ash: Kinetic and Equilibrium Studies. *J. Hazard. Mater.* **2008**, *150*, 737–746. [CrossRef]
57. Eren, Z.; Acar, F.N. Adsorption of Reactive Black 5 from an Aqueous Solution: Equilibrium and Kinetic Studies. *Desalination* **2006**, *194*, 1–10. [CrossRef]
58. Hameed, B.H.; Rahman, A.A. Removal of Phenol from Aqueous Solutions by Adsorption onto Activated Carbon Prepared from Biomass Material. *J. Hazard. Mater.* **2008**, *160*, 576–581. [CrossRef]
59. Sen, T.K.; Afroze, S.; Ang, H.M. Equilibrium, Kinetics and Mechanism of Removal of Methylene Blue from Aqueous Solution by Adsorption onto Pine Cone Biomass of Pinus Radiata. *Water. Air. Soil Pollut.* **2011**, *218*, 499–515. [CrossRef]
60. Elmoubarki, R.; Mahjoubi, F.Z.; Tounsadi, H.; Moustadraf, J.; Abdennouri, M.; Zouhri, A.; El Albani, A.; Barka, N. Adsorption of Textile Dyes on Raw and Decanted Moroccan Clays: Kinetics, Equilibrium and Thermodynamics. *Water Resour. Ind.* **2015**, *9*, 16–29. [CrossRef]
61. Collivignarelli, M.C.; Abbà, A.; Miino, M.C.; Damiani, S. Treatments for Color Removal from Wastewater: State of the Art. *J. Environ. Manage.* **2019**, *236*, 727–745. [CrossRef] [PubMed]
62. Awfa, D.; Ateia, M.; Fujii, M.; Johnson, M.S.; Yoshimura, C. Photodegradation of Pharmaceuticals and Personal Care Products in Water Treatment Using Carbonaceous-TiO_2 Composites: A Critical Review of Recent Literature. *Water Res.* **2018**, *142*, 26–45. [CrossRef] [PubMed]
63. Zhang, X.; Wang, Y.; Liu, B.; Sang, Y.; Liu, H. Heterostructures Construction on TiO_2 Nanobelts: A Powerful Tool for Building High-Performance Photocatalysts. *Appl. Catal. B Environ.* **2017**, *202*, 620–641. [CrossRef]
64. Lan, Y.; Lu, Y.; Ren, Z. Mini Review on Photocatalysis of Titanium Dioxide Nanoparticles and Their Solar Applications. *Nano Energy* **2013**, *2*, 1031–1045. [CrossRef]
65. Ameh, A.E.; Fatoba, O.O.; Musyoka, N.M.; Petrik, L.F. Influence of Aluminium Source on the Crystal Structure and Framework Coordination of Al and Si in Fly Ash-Based Zeolite NaA. *Powder Technol.* **2017**, *306*, 17–25. [CrossRef]
66. Isac, L.; Andronic, L.; Enesca, A.; Duta, A. Copper Sulfide Films Obtained by Spray Pyrolysis for Dyes Photodegradation under Visible Light Irradiation. *J. Photochem. Photobiol. A Chem.* **2013**, *252*, 53–59. [CrossRef]
67. Cheung, W.H.; Szeto, Y.S.; McKay, G. Intraparticle Diffusion Processes during Acid Dye Adsorption onto Chitosan. *Bioresour. Technol.* **2007**, *98*, 2897–2904. [CrossRef]
68. Ozawa, M.; Matsui, H.; Suzuki, S. Formation of TiO_2/Mica Composite for Photocatalysis. *Powder Metall. Met. Ceram.* **2016**, *54*, 746–749. [CrossRef]
69. Shalan, A.E.; Rasly, M.; Rashad, M.M. Organic Acid Precursor Synthesis and Environmental Photocatalysis Applications of Mesoporous Anatase TiO_2 Doped with Different Transition Metal Ions. *J. Mater. Sci. Mater. Electron.* **2014**, *25*, 3141–3146. [CrossRef]
70. Qian, Z.; Pathak, B.; Nisar, J.; Ahuja, R. Oxygen- and Nitrogen-Chemisorbed Carbon Nanostructures for Z-Scheme Photocatalysis Applications. *J. Nanopart. Res.* **2012**, *14*, 895. [CrossRef]
71. Lim, P.F.; Leong, K.H.; Sim, L.C.; Abd Aziz, A.; Saravanan, P. Amalgamation of N-Graphene Quantum Dots with Nanocubic like TiO_2: An Insight Study of Sunlight Sensitive Photocatalysis. *Environ. Sci. Pollut. Res.* **2019**, *26*, 3455–3464. [CrossRef] [PubMed]
72. Xiang, D.; Qu, F.; Chen, X.; Yu, Z.; Cui, L.; Zhang, X.; Jiang, J.; Lin, H. Synthesis of Porous ZnO Nanospheres for Gas Sensor and Photocatalysis. *J. Sol-Gel Sci. Technol.* **2014**, *69*, 370–377. [CrossRef]
73. Lü, W.; Chen, J.; Wu, Y.; Duan, L.; Yang, Y.; Ge, X. Graphene-Enhanced Visible-Light Photocatalysis of Large-Sized CdS Particles for Wastewater Treatment. *Nanoscale Res. Lett.* **2014**, *9*, 148. [CrossRef] [PubMed]
74. Sun, Z.; He, X.; Du, J.; Gong, W. Synergistic Effect of Photocatalysis and Adsorption of Nano-TiO_2 Self-Assembled onto Sulfanyl/Activated Carbon Composite. *Environ. Sci. Pollut. Res.* **2016**, *23*, 21733–21740. [CrossRef] [PubMed]
75. Sheng, Y.; Wei, Z.; Miao, H.; Yao, W.; Li, H.; Zhu, Y. Enhanced Organic Pollutant Photodegradation via Adsorption/Photocatalysis Synergy Using a 3D g-C_3N_4/TiO_2 Free-Separation Photocatalyst. *Chem. Eng. J.* **2019**, *370*, 287–294. [CrossRef]
76. Li, H.; Ho, W.; Cao, J.; Park, D.; Lee, S.; Huang, Y. Active Complexes on Engineered Crystal Facets of MnO_x –CeO_2 and Scale-Up Demonstration on an Air Cleaner for Indoor Formaldehyde Removal. *Environ. Sci. Technol.* **2019**, *53*, 10906–10916. [CrossRef]

77. Bokare, A.D.; Choi, W. Review of Iron-Free Fenton-like Systems for Activating H_2O_2 in Advanced Oxidation Processes. *J. Hazard. Mater.* **2014**, *275*, 121–135. [CrossRef]
78. Zhang, M.; Dong, H.; Zhao, L.; Wang, D.; Meng, D. A Review on Fenton Process for Organic Wastewater Treatment Based on Optimization Perspective. *Sci. Total Environ.* **2019**, *670*, 110–121. [CrossRef]
79. Fodor, S.; Baia, L.; Hernádi, K.; Pap, Z. Controlled Synthesis of Visible Light Active CuxS Photocatalyst: The Effect of Heat Treatment on Their Adsorption Capacity and Photoactivity. *Materials (Basel)* **2020**, *13*, 3665. [CrossRef]